Correction for Synchronization Errors in Dynamic Measurements

Vasishta Ganguly and Tony L. Schmitz
Department of Mechanical Engineering and Engineering Science
University of North Carolina at Charlotte
Charlotte, NC, USA

ABSTRACT
In modal testing, an impulse may be used to excite the structure and a linear transducer may be applied to measure the corresponding response. For these impact tests, two signals are measured: the impulsive force and the vibration response. Any lack of synchronization in the time domain acquisition of the two signals results in a frequency-dependent phase error in the frequency response function (FRF). However, knowledge of this phase error obtained from separate tests may be used to correct the measurement phase error. In this research, two techniques to measure the frequency-dependent phase error are discussed and a frequency domain technique is proposed to correct the FRF. The phase error for both a capacitive sensor and a laser Doppler vibrometer was determined. The correction method was validated using an FRF measurement of a cylindrical artifact mounted in a milling machine spindle.

KEYWORDS
Dynamics, phase, modal, time delay, capacitance gage, vibrometer, accelerometer

INTRODUCTION

It is often necessary to identify the dynamic response of structures. Examples include bridges, automobiles, machine tools, and measuring instruments. The dynamic response of mechanical structures may be represented by the complex-valued frequency response function (FRF). The FRF defines the vibration output to force input ratio in the frequency domain [1]. It represents the steady-state (particular) solution to the system differential equation of motion. The FRF is characterized by either the frequency-dependent magnitude and phase, or the real and imaginary parts. The FRF of a structure may be measured using modal testing [1]. In one type of modal testing, referred to as impact testing, an impulse force is applied to a structure and a linear transducer is used to measure the response. The displacement, velocity, or acceleration may be used to identify the FRF.

Capacitance gages and laser Doppler vibrometers (LDV) are non-contact sensors which offer high bandwidth and resolution. These sensors may be used for displacement/velocity feedback, spindle error motion characterization, and frequency response measurements in structural dynamics testing. They employ amplifying electronics to convert the change in displacement/velocity to a proportional voltage which may then be sampled by a data acquisition (DAQ) system. Depending on its design, the amplifier can induce a time delay in the measurement signal, i.e., there is a small time delay between the input displacement/velocity of the target and the output voltage from the amplifier. For example, analog low pass filters used to attenuate high frequency noise are often incorporated in the amplifying electronics. These filters can introduce a time delay. These time delays lead to frequency-dependent phase errors in the FRF. Furthermore, the digital DAQ system may introduce some synchronization errors between the force and response signals, which again result in a phase error.

In this research, an experimental technique to identify the frequency-dependent phase error is described. The technique may also be extended to identify synchronization errors due to the DAQ system. A frequency domain approach is proposed to correct the FRF for the phase errors. The method is verified using a cylindrical artifact mounted in a milling machine spindle.

FREQUENCY RESPONSE FUNCTION

For a lumped parameter[1] single degree of freedom spring-mass-damper system with a harmonic force input, the time domain equation of motion is:

[1] In a lumped parameter system, the mass is concentrated at the coordinate that describes the system motion and the spring and damper are assumed to be massless.

$$m\ddot{x} + c\dot{x} + kx = Fe^{i\omega t}, \quad (1)$$

where m is the mass, c is the viscous damping coefficient, k is the stiffness, and $f(t) = Fe^{i\omega t}$ is the force (ω is the forcing frequency in rad/s). Also, $x(t)$ is the displacement, $\dot{x}(t)$ is the velocity, and $\ddot{x}(t)$ is the acceleration.

The total solution to the forced vibration equation of motion (Eq. 1) has two parts: the homogeneous, or transient, solution; and the particular, or steady-state, solution. The steady-state portion remains after the transient has attenuated and it persists as long as the force is acting on the system. The particular solution takes the same form as the forcing function. The resulting vibration has the same frequency as the harmonic force. Specifically, given the force $f(t) = Fe^{i\omega t}$, the corresponding steady-state response can be written as $x(t) = Xe^{i\omega t}$. Given this form for the position, the velocity is $\dot{x}(t) = i\omega Xe^{i\omega t}$ and the acceleration is $\ddot{x}(t) = (i\omega)^2 Xe^{i\omega t} = -\omega^2 Xe^{i\omega t}$. Substituting these expressions in Eq. 1 gives:

$$\left(-m\omega^2 + i\omega c + k\right) Xe^{i\omega t} = Fe^{i\omega t}. \quad (2)$$

Equation 2 relates the force to the resulting vibration as a function of the forcing frequency, ω. Rewriting gives the ratio of the output (the complex-valued vibration, X) to the input (the real-valued force, F); this is the FRF for the system [2].

$$\frac{X}{F}(\omega) = \frac{1}{-m\omega^2 + i\omega c + k} \quad (3)$$

Equation 3 can be rewritten using the frequency ratio, $r = \omega/\omega_n$, where $\omega_n = \sqrt{k/m}$ (rad/s) is the (undamped) natural frequency, and dimensionless damping ratio, $\zeta = c/2\sqrt{km}$; see Eq. 4. The FRF is typically represented as either the real, $\mathrm{Re}\left(\frac{X}{F}(r)\right)$, and imaginary, $\mathrm{Im}\left(\frac{X}{F}(r)\right)$, parts or, alternately, the magnitude, $\left|X/F(r)\right|$, and phase, $\phi(r)$. See Eqs. 5-8.

$$\frac{X}{F}(r) = \frac{1}{k}\left(\frac{1}{(1-r^2) + i2\zeta r}\right) = \frac{1}{k}\left(\frac{(1-r^2) - i2\zeta r}{(1-r^2)^2 + (2\zeta r)^2}\right) \quad (4)$$

$$\mathrm{Re}\left(\frac{X}{F}(r)\right) = \frac{1}{k}\left(\frac{(1-r^2)}{(1-r^2)^2 + (2\zeta r)^2}\right) \quad (5)$$

$$\mathrm{Im}\left(\frac{X}{F}(r)\right) = \frac{1}{k}\left(\frac{-2\zeta r}{(1-r^2)^2 + (2\zeta r)^2}\right) \quad (6)$$

$$\left|\frac{X}{F}(r)\right| = \sqrt{\left(\mathrm{Re}\left(\frac{X}{F}(r)\right)\right)^2 + \left(\mathrm{Im}\left(\frac{X}{F}(r)\right)\right)^2}$$

$$\left|\frac{X}{F}(r)\right| = \frac{1}{k}\sqrt{\frac{1}{(1-r^2)^2 + (2\zeta r)^2}} \quad (7)$$

$$\phi(r) = \tan^{-1}\left(\frac{\mathrm{Im}\left(\frac{X}{F}(r)\right)}{\mathrm{Re}\left(\frac{X}{F}(r)\right)}\right) = \tan^{-1}\left(\frac{-2\zeta r}{1-r^2}\right) \quad (8)$$

The relationships between the real/imaginary parts and the magnitude/phase are conveniently defined in the complex plane as shown in Fig. 1. Based on this vector representation of the FRF at a particular r value, it is seen that a phase error will affect both the Re and Im values.

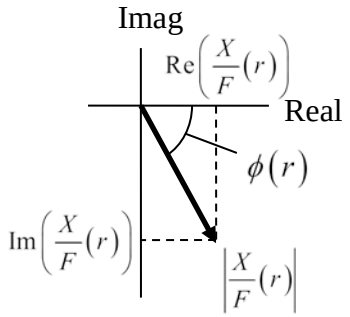

Figure 1. Vector description of the relationships between the real/imaginary parts and magnitude/phase. The phase indicates the complex displacement lag relative to the force (real-valued and pointing to the right along the Real axis).

Time delay

Next, consider the effect of a time delay between the actual system response and the measured vibration. This can be introduced, for example, by the amplifying/signal conditioning electronics that convert the transducer output to the voltage that is subsequently sampled and converted from the time domain to the frequency domain for the FRF computation. As shown schematically in Fig. 2, the measurement signal may be time delayed by a small amount relative to the actual vibration. For a constant time delay, this yields a phase error that increases linearly with frequency. Figure 3 displays the actual, x_a, and measured, x_m, signals for a 50 ms time delay at three different oscillating frequencies, f, of {1, 2, and 3} Hz. The

corresponding phase errors are {-18, -36, and -54} deg. The phase error was calculated using Eq. 9.

$$\Delta\phi(f) = \cos^{-1}\left(\frac{x_a x_m}{|x_a||x_m|}\right) \quad (9)$$

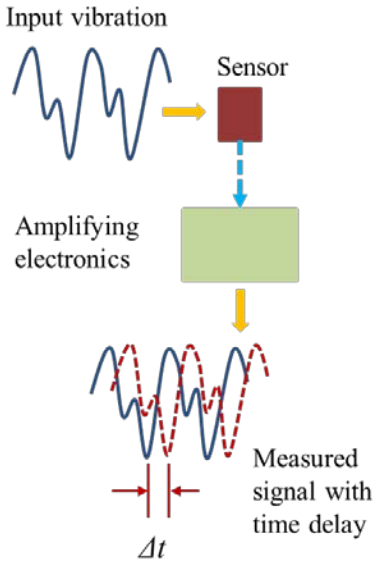

Figure 2. Schematic representation of time delay between actual and measured vibration signals.

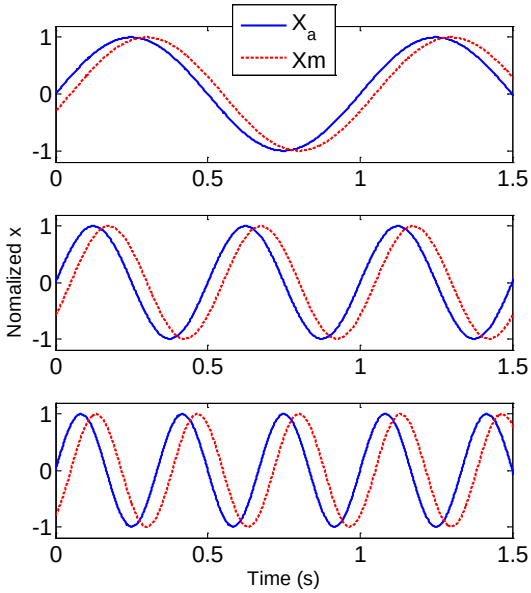

Figure 3. Effect of 50 ms time delay on phase: (top) 1 Hz frequency gives a -18 deg phase lag; (middle) 2 Hz frequency gives a -36 deg phase lag; and (bottom) 3 Hz frequency gives a -54 deg phase lag.

Using Eq. 9, the frequency-dependent phase error can be calculated for any time delay between x_a and x_m. Figure 4 shows the linearly-varying phase error for a range of time delays from 10 μs to 90 μs. The slope for each linear trend is listed in the legend. It is seen that a 50 μs delay gives a slope of -18 deg/kHz and, therefore, a -90 deg phase error at 5000 Hz. Using Fig. 1, it is observed that a -90 deg phase error switches the amplitudes of the real and imaginary parts and changes the sign of the imaginary part.

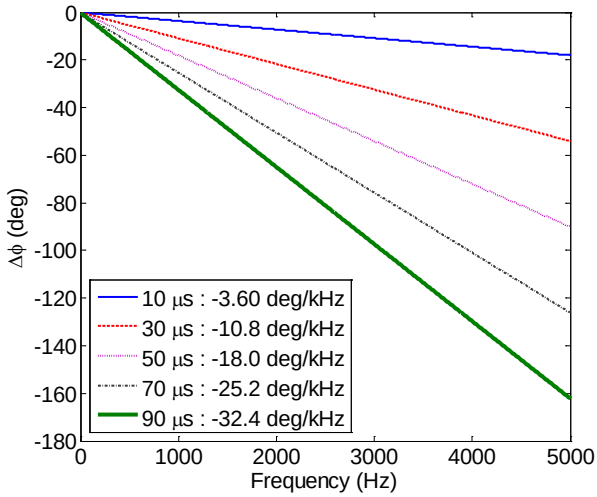

Figure 4. Phase error for different time delays.

EXPERIMENTAL SETUP

Two different methods were employed to evaluate the frequency-dependent phase errors: a) frequency sweep test; and b) broadband excitation.

Frequency Sweep Test

Figure 5 shows a schematic representation of the measurement setup. In the frequency sweep test, the measurement bandwidth was divided into a number of discrete steps and the phase error was measured independently at each frequency. The target was oscillated using a modal shaker (TIRAvib 51075) capable of generating oscillations up to 5000 Hz. A function generator (Hewlett Packard 33120A) was used to drive the shaker at the desired fixed frequency. The target motion was measured using three different linear transducers. The target acceleration was measured using a low-mass integrated circuit PZT (ICP) accelerometer (PCB 352C23). The accelerometer signal was amplified using a PCB 482A16 signal conditioner. The target velocity was measured using a laser Doppler vibrometer (Polytec OFV-534) controlled using a Polytec OFV-5000 controller. The target displacement was measured using a capacitance gage sensor (Lion Precision C23 B). The capacitance gage signal was amplified using a Lion Precision CPL 290 Elite series amplifier. Data was acquired at 100 kHz using a National

Instruments (NI) 9215 DAQ card mounted in a NI compact DAQ chassis (NI cDAQ 9714). The accelerometer signal was used as the reference signal with respect to which the phase error was measured. The amplifying electronics for the accelerometer do not introduce any phase errors in the amplified accelerometer voltage signal up to the resonant frequency of the accelerometer (70 kHz for the PCB 352C23 accelerometer). This resonant frequency is higher than the bandwidth of interest. Measurements were conducted over a frequency range of 100 Hz to 5000 Hz in 25 Hz increments. The measured data was digitally filtered using a third-order band pass filter with a bandwidth of 100 Hz centered at the oscillation frequency.

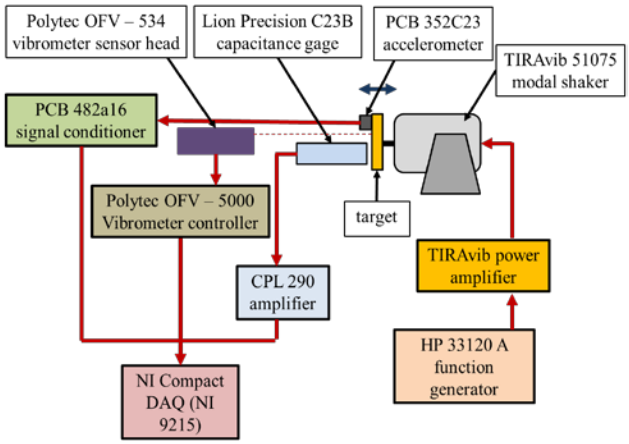

Figure 5. Schematic representation of experimental setup for frequency sweep test (top).

Figure 6 shows a plot of 100 Hz simulated acceleration, velocity and displacement signals. The vertical axis is normalized to give a unit magnitude for each. Additionally, delayed displacement and velocity signals with a phase lag of 30 deg are also shown. Note that the acceleration lags velocity by π/2 rad (90 deg) and displacement by π rad (180 deg).

The amplifier induced phase error, ϕ_{disp} (deg), between the sinusoidal acceleration and displacement signals, *a* and *x*, with frequency, *f*, may be calculated using,

$$\phi_{disp}(f) = \cos^{-1}\left(\frac{x.a}{|x||a|}\right) - 180\,. \qquad (10)$$

The amplifier induced phase error, ϕ_{vel} (deg), between the sinusoidal acceleration and velocity signals, *a* and *v*, with frequency, *f*, may be calculated using,

$$\phi_{vel}(f) = 90 - \cos^{-1}\left(\frac{v.a}{|v||a|}\right). \qquad (11)$$

The capacitance gage amplifier and the vibrometer controller may be operated using different low pass filter settings. The frequency-dependent phase errors differ depending on the amplifier setting. Furthermore, the phase errors in the vibrometer are sensitive to the operating range of the controller. In this study, the tests were performed with the vibrometer controller set to an operating range of 50 mm/s/V. The capacitance gage and vibrometer results are reported in Tables 1 and 2, respectively. Figures 7 and 8 show the measured phase errors as well as the best fit lines for the capacitance gage and vibrometer, respectively.

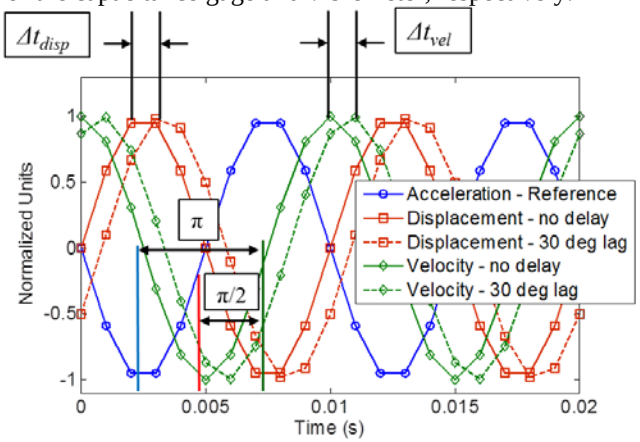

Figure 6. Normalized plot of acceleration, displacement and velocity illustrating the inherent phase difference.

Table 1. Frequency-dependent phase error for capacitance gage measurements.

Low pass filter (kHz)	Phase error (deg/kHz)
15	-13.84
10	-20.00
1	-73.27

Table 2. Frequency-dependent phase error for vibrometer measurements.

Low pass filter (kHz)	Phase error (deg/kHz)
Off	-5.32
1500	-5.37
100	-6.25
20	-10.27
5	-25.25

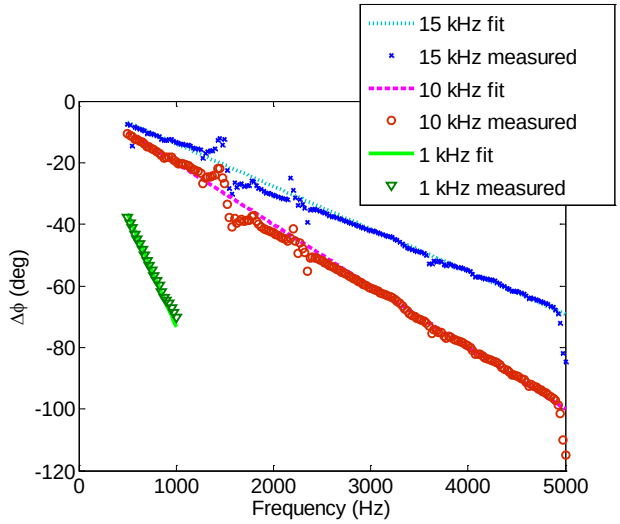

Figure 7. Phase error between accelerometer and capacitance gage at different low pass filter settings.

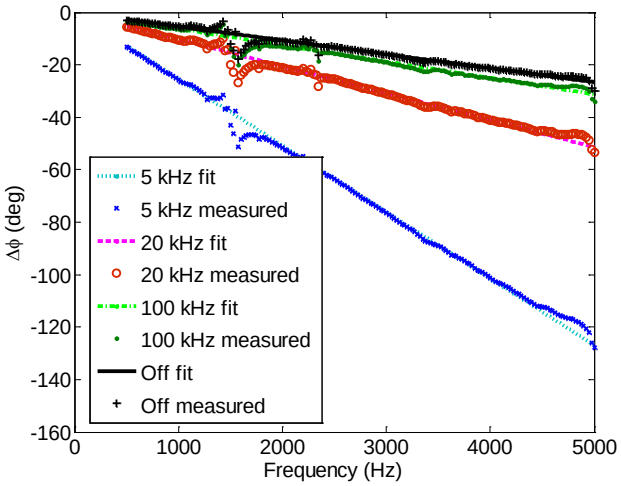

Figure 8. Phase error between accelerometer and vibrometer at different low pass filter settings.

Deviations from the best fit line were observed in the 1500 Hz to 2000 Hz region. These deviations were attributed to the rotary modes of vibration of the target at certain frequencies. To identify these modes, an impact test was performed on the target with the shaker active. Figure 9 shows the experimental setup. An impulse force was applied at one end of the target and the response was measured on the opposite end. In this manner, the rotation of the target with respect to the applied force was measured. Figure 10 shows the real and imaginary parts of the measured FRF. The rotary modes of the target are clearly observed near 1500 Hz. These modes contribute to the nonlinear deviations in the measured phase lag observed in Figs. 7 and 8.

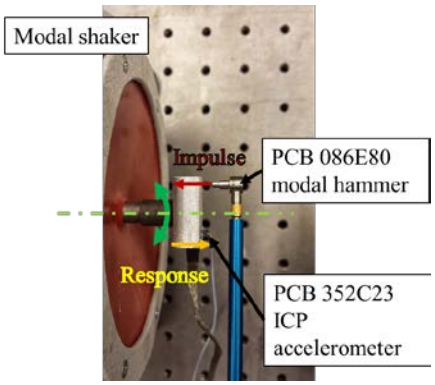

Figure 9. Experimental setup to measure rotary modes of vibration of the shaker.

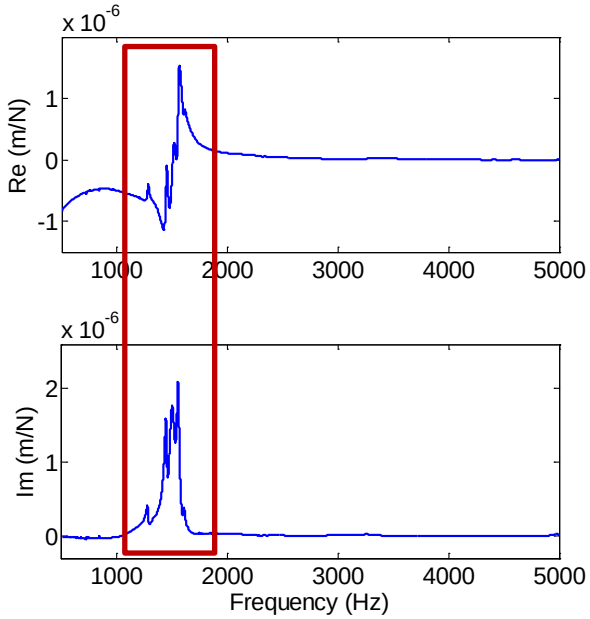

Figure 10. Real and imaginary parts of measured shaker FRF. The plot shows the rotary modes near 1500 Hz.

Broadband Excitation

Figure 11 shows the measurement setup. An impulse force, applied using a modally tuned hammer (PCB 086C04), was used to excite a flexure over a wide frequency range. The response of the flexure was simultaneously measured using the same accelerometer (PCB 352C23), the vibrometer, and capacitance gage. Again, the accelerometer signal was used as the reference signal for the phase error evaluation. The FRF can be expressed in terms of the displacement, velocity, and acceleration signals as:

$$FRF(f) = \frac{X(f)}{F(f)} = \frac{1}{i\omega}\frac{V(f)}{F(f)} = -\frac{1}{\omega^2}\frac{A(f)}{F(f)}, \quad (12)$$

where $X(f)$, $V(f)$, $A(f)$, and $F(f)$ are the Fourier transforms of the displacement, velocity, acceleration, and force signals,

respectively, and *f* is the frequency in Hz. The phase errors introduced by the capacitance gage and vibrometer amplifying electronics are identified in the frequency domain by comparison with the accelerometer phase.

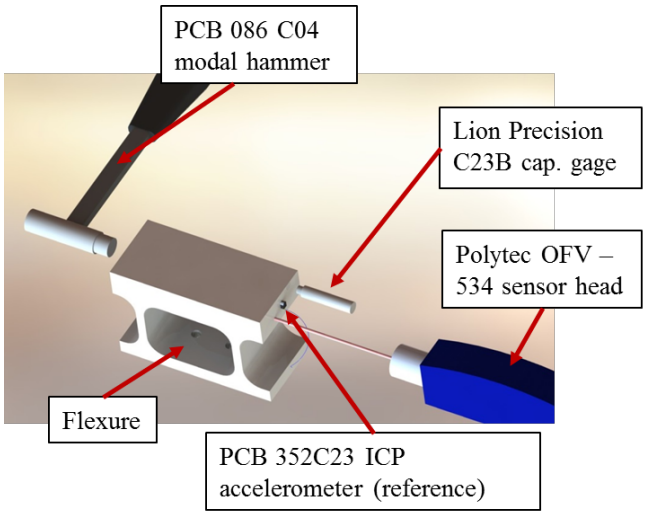

Figure 11. Schematic representation of experimental setup for broadband excitation test (top).

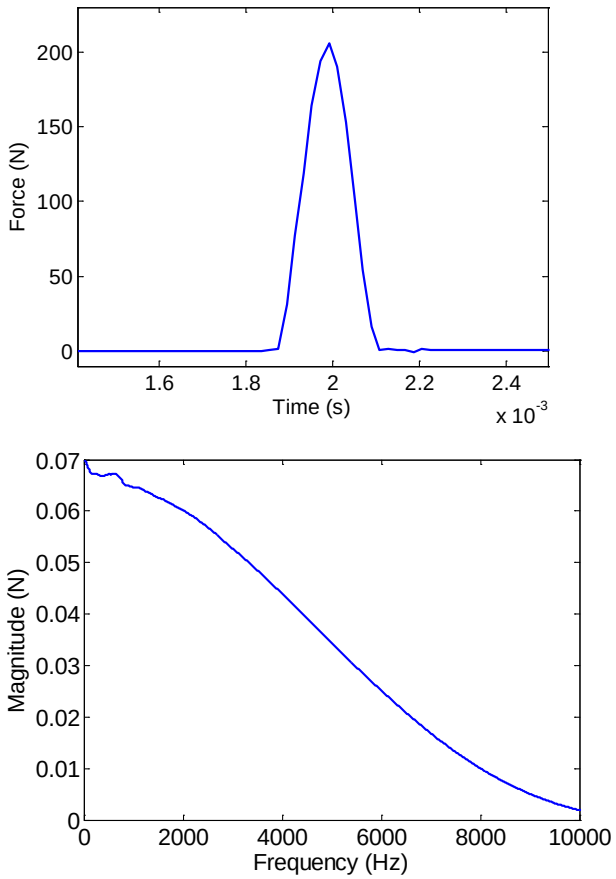

Figure 12. Magnitude of impulse force represented in the time domain (top) and in the frequency domain (bottom).

The excitation bandwidth is inversely related to the impulse period, while the excitation magnitude is directly related to the magnitude of the impulse force. Figure 12 shows a plot of the impulse force in the time domain (top) and in the frequency domain (bottom) to provide an estimate of the excited bandwidth.

Figure 13 shows the first two modes of vibration of the flexure. The three sensors simultaneously measure the dynamics response at different locations on the side of the flexure as shown in Figure 11. The response measured by the three sensors around the first natural frequency (1708 Hz) has the same magnitude and phase. However, for the second (twisting mode) natural frequency (3400 Hz), the response measured by the three sensors is not necessarily identical. Therefore, the frequency range from 3200 Hz to 3600 Hz was ignored when comparing the phase of the three sensors.

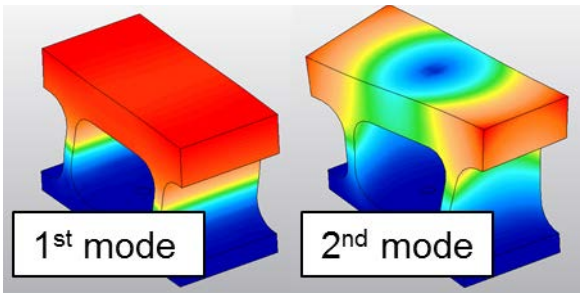

Figure 13. First two vibration modes for the flexure.

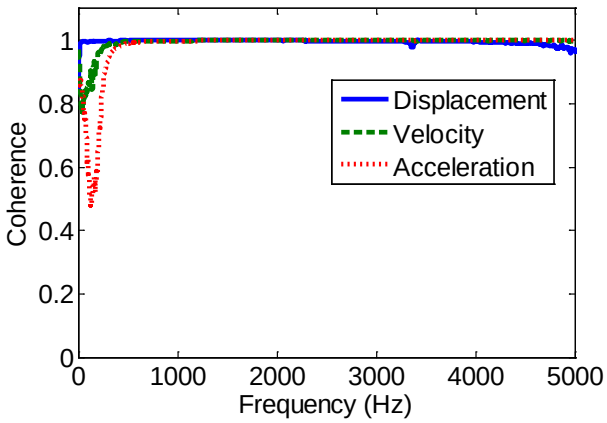

Figure 14. First two vibration modes for the flexure.

The coherence of an FRF provides an estimate of the reliability of the measurement [1]. Ideally, the coherence is unity. Figure 14 shows a plot of the FRF coherence for the three sensors. It is less than one at low frequencies for the accelerometer and vibrometer due to the frequency domain integration (see Eq. 12). It was also observed that the coherence drops near the second natural frequency. The phase error was only calculated for frequency values where the coherence was greater than 0.95.

Figure 15 shows the mean phase for the three sensors from 12 repetitions. It is observed that the phase for both the capacitance gage (CG) and the vibrometer (LDV) lags the accelerometer phase. The frequency-dependent phase error is calculated using:

$$\phi_{err_{CG}}(f) = \angle\left(\frac{X(f)}{F(f)}\right) - \angle\left(-\frac{1}{\omega^2}\frac{A(f)}{F(f)}\right) \text{ and}$$

$$\phi_{err_{LDV}}(f) = \angle\left(\frac{1}{i\omega}\frac{V(f)}{F(f)}\right) - \angle\left(-\frac{1}{\omega^2}\frac{A(f)}{F(f)}\right), \quad (13)$$

where∠ represents the FRF phase. Figure 16 shows the frequency dependent phase error for the capacitance gage and vibrometer measurements. Within the measurement range, the phase error was found to change linearly with frequency. The slope of the linear fit was used to characterize the phase error as shown in Table 3.

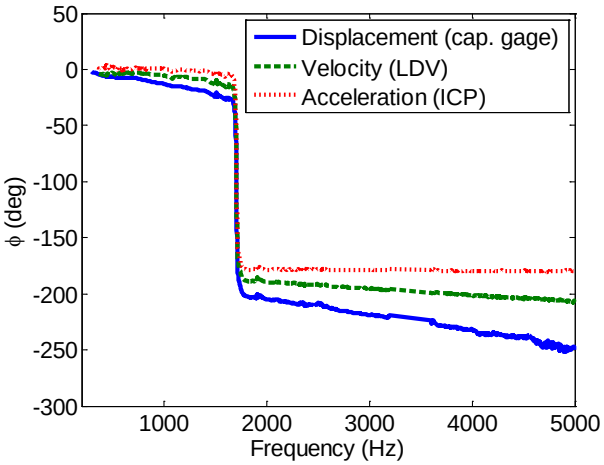

Figure 15. FRF phase: displacement (cap. gage), velocity (laser Doppler vibrometer, or LDV), and acceleration (ICP).

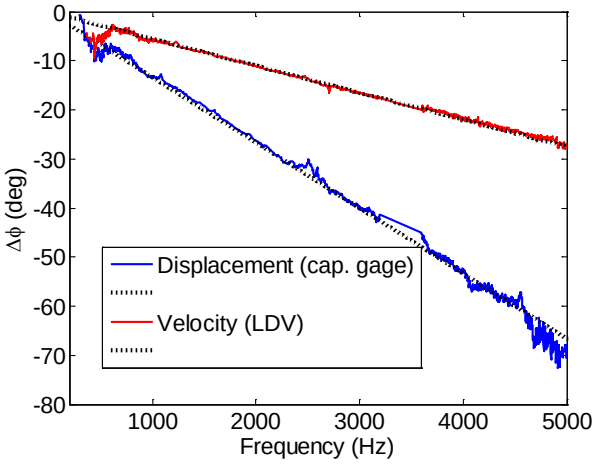

Figure 16. Phase error for the capacitance gage and LDV with reference to the accelerometer.

Table 3. Frequency-dependent phase error measured using broadband excitation.

Instrument	Frequency dependent phase error (deg/kHz)	
	Mean	Standard deviation
Broadband excitation		
Capacitance gage (15 kHz)	-13.54	0.17
Vibrometer (filter off)	-5.47	0.13

SYNCHRONIZATION ERRORS IN DAQ SYSTEMS

In this study, a compact data acquisition system (NI cDAQ 9174) was used to collect the data. Two different cards (NI 9215 and NI 9324) were mounted in the same cDAQ chassis. The NI 9215 is capable of measuring a voltage signal within a range of ±10 V at a sampling rate of up to 100 kHz. The NI 9324 can measure a voltage signal within the range of ±5 V at a sampling rate of up to 51.2 kHz. The NI 9324 also provides the necessary supply current for integrated circuit PZT (ICP) sensors, such as accelerometers and modal hammers. Individually, each card has four channels which are sampled simultaneously. However, the different cards mounted within the same cDAQ chassis are not necessarily synchronized. Synchronization errors between the different channels of the data acquisition system must be taken into account when measuring dynamic response data.

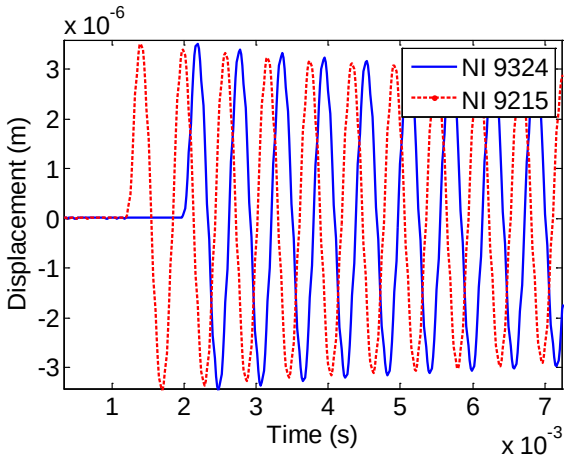

Figure 17. Synchronization error in data acquired by two DAQ cards (NI 9215 and NI 9324).

To measure the DAQ system-induced synchronization error, the same displacement (response) signal from the capacitance gage was split and was simultaneously collected by both the DAQ cards (NI 9215 and NI 9324)

mounted in the cDAQ chassis. Figure 17 shows a time domain plot of the identical response signal acquired by the two different DAQ cards. The measurement data acquired by the NI 9215 card leads that acquired by the NI 9324 card. In the frequency domain, the phase delay introduced by the data acquisition system may be estimated as:

$$\phi_{err_{DAQ}}(f) = \angle\left[\frac{X_{NI\,9324}(f)}{X_{NI\,9215}(f)}\right], \qquad (14)$$

where $X_{NI\ 9324}(f)$ and $X_{NI\ 9215}(f)$ represent the Fourier transform of the response signal acquired by the NI 9324 and NI 9215 DAQ cards, respectively. Figure 18 shows the DAQ phase error as a function of frequency. Note that the error is reset to zero each time it is crosses 360 deg. The NI 9324 card lags the NI 9215 card.

When measuring the FRF of a mechanical structure, it is necessary to account for the synchronization errors introduced due to the DAQ system as well as the sensor electronics. In this example, the dynamic response of the flexure assembly was measured. The input impulse force signal from the modal hammer was collected by the ICP compatible NI 9324 card and the capacitance gage response signal was collected by the NI 9215 card. Note that in this case, the impulse data (NI9324) lags the response data (NI9215) which is physically impossible. Also, the capacitance gage amplifier introduced a time delay in the response signal. The phase lag introduced by the capacitance gage amplifier was smaller than the phase lead introduced by the DAQ system. Both these factors were considered when correcting the FRF. Figure 19 shows the net effect of the phase errors introduced by the DAQ system and the capacitance gage amplifier. Figure 20 shows measured and corrected phases for the FRF measurement. The cumulative phase correction is the sum of phase lead due the DAQ system (Eq. 14) and the phase lag due to the capacitance gage amplifier (Eq. 13). The cumulative phase correction may be estimated as:

$$\phi_{err_{cumulative}}(f) = \phi_{err\ DAQ}(f) + \phi_{err_{CG}}(f), \qquad (14)$$

PHASE CORRECTION ALGORITHM

Given the frequency-dependent phase errors, the effect of the time delay can be removed from the measured FRF. The measured phase, ϕ_m, is corrected by subtracting the phase error, $\Delta\phi$, which is determined from the product of the slope, *S*, from Fig. 8, (deg/Hz), and the frequency, *f* (Hz). See Eq. 16, where ϕ_c is the corrected phase.

$$\phi_c(f) = \phi_m - \Delta\phi = \phi_m - S \cdot f \qquad (16)$$

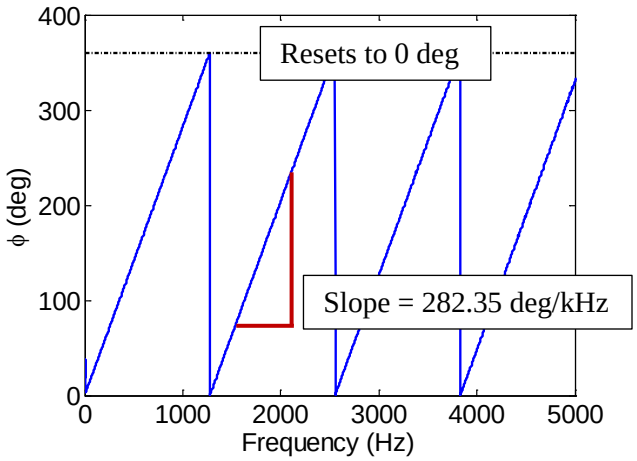

Figure 18. DAQ induced phase error

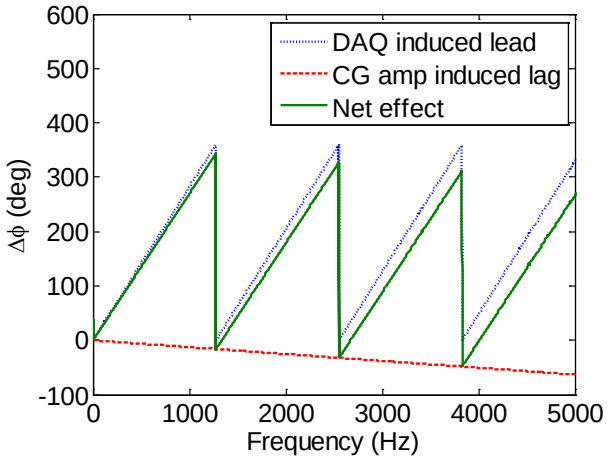

Figure 19. Net effect of DAQ and amplifier-induced phase errors.

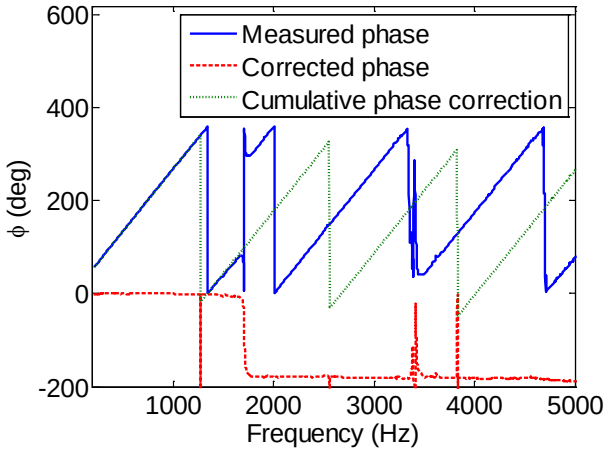

Figure 20. Measured and corrected phase of flexure FRF.

The real and imaginary parts of the measured FRF are then corrected using ϕ_c. See Eqs. 17 and 18, where it is

assumed that the FRF magnitude is not affected by the time delay.

$$\mathrm{Re}\left(\frac{X}{F}(f)\right)_c = \left|\frac{X}{F}(f)\right|\cos\left(\phi_c(f)\right) \tag{17}$$

$$\mathrm{Im}\left(\frac{X}{F}(f)\right)_c = \left|\frac{X}{F}(f)\right|\sin\left(\phi_c(f)\right) \tag{18}$$

To demonstrate the correction algorithm, FRF tests were performed on a cylindrical artifact (a modified boring bar blank) mounted in the spindle of a Haas TM-1 CNC vertical machining center (CAT-40 interface). Figure 21 displays a photograph of the experimental setup. A modally-tuned hammer (PCB 086C04) was used to excite the structure and the response was measured at the free end of the artifact using both the capacitive sensor and accelerometer. The data for all three sensors was acquired simultaneously at a 100 kHz sampling rate using the NI DAQ.

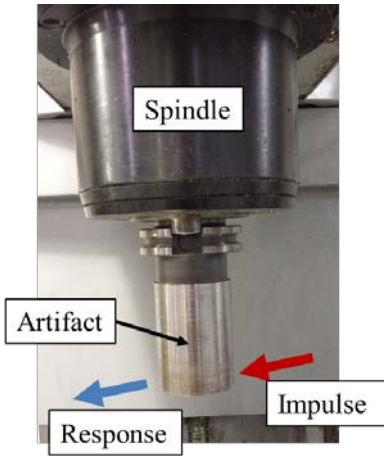

Figure 21. Experimental setup. Cylindrical artifact mounted in the Haas TM1 spindle.

Figure 22 shows the magnitude and phase of the measured and corrected FRFs obtained using the capacitive sensor. The FRF obtained using the ICP accelerometer is also shown. The real and imaginary parts are plotted in Fig 23. Note that the uncorrected capacitive sensor measurement deviates from the accelerometer FRF at higher frequencies. In particular, for the mode near 4300 Hz in the uncorrected capacitive sensor FRF, the measured (dashed line) real part resembles the imaginary part of an error-free mode and the imaginary part resembles the inverted real part of an error-free mode. Smaller differences are also observed for the lower frequency modes. However, the corrected capacitive sensor result (dotted line) matches the accelerometer result (solid line).

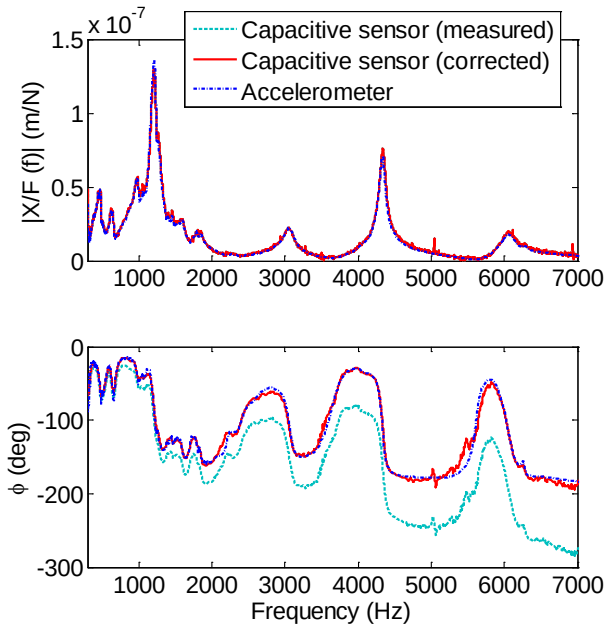

Figure 22. Artifact FRF comparison: magnitude (top) and phase (bottom).

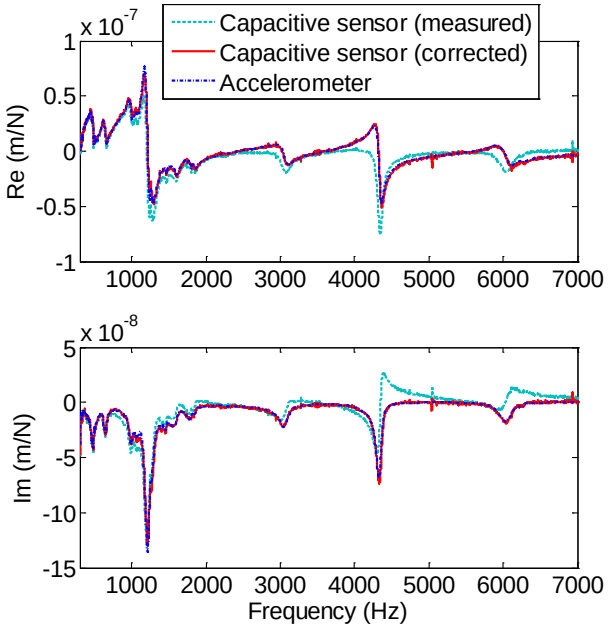

Figure 23. Artifact FRF comparison: real (top) and imaginary (bottom) parts.

CONCLUSIONS

In this study, the frequency-dependent phase error introduced by the amplifying electronics was identified for a capacitance gage and a laser Doppler vibrometer. Synchronization errors introduced by the data acquisition system were also identified. A frequency domain technique

to correct the phase error was described and applied to FRF measurements of a cylindrical artifact mounted in a milling machine spindle. The measurements showed that the corrected FRFs agreed with the FRF measured using the accelerometer.

REFERENCES

[1] Ewins D.J, 2000, Modal Testing: Theory, Practice and Application, 2nd ed., Research Studies Press LTD, Hertfordshire.
[2] Schmitz, T. and Smith, K.S., 2012, Mechanical Vibrations: Modeling and Measurement, Springer, New York.
[3] http://www.lionprecision.com/tech-library/technotes/cap-0020-sensor-theory.html.
[4] Lion Precision, 2011, TechNote LT03-0031 EliteSeries Amplitude/Phase Frequency Response.